# Morphometric analysis of the terminal ductal lobular unit architecture in human breast

Markus Peurla[1,2,*], Oona Paavolainen[1,2,*], Ella Tammelin[1,2], Suvi-Riitta Sulander[1,2], Larissa Mourao[3], Pia Boström[4,5], Nina Brück[4,5] Colinda LGJ Scheele[3], Pauliina Hartiala[5,6,7] and Emilia Peuhu[1,2,#]

[1]Institute of Biomedicine, Cancer Laboratory FICAN west, University of Turku, Turku, Finland
[2]Turku Bioscience, University of Turku and Åbo Akademi University, Turku, Finland
[3]VIB Center for Cancer Biology, Department of Oncology, KU Leuven, Leuven, Belgium
[4]Department of Pathology, Turku University Hospital, Turku, Finland
[5]University of Turku, Turku, Finland
[6]Department of Plastic and General Surgery, Turku University Hospital, Turku, Finland
[7]Medicity Research Laboratories and InFLAMES Research Flagship Center, University of Turku, Turku, Finland
*Equal Contribution
[#]Lead author

## Graphical Abstract

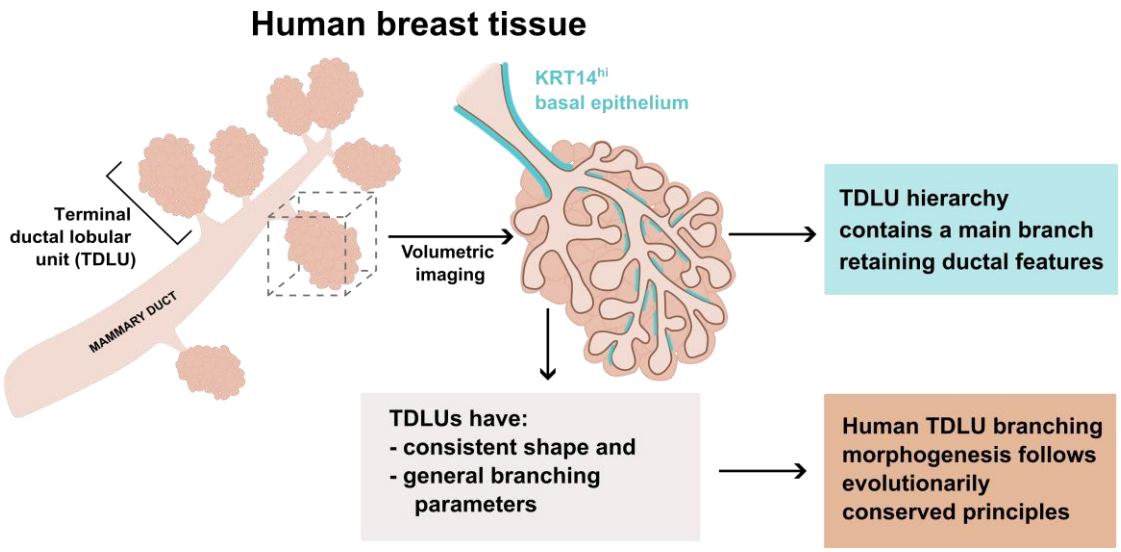


## Abstract

The major lactiferous ducts of the human breast branch out and ultimately end at terminal ductal lobular units (TDLUs). These glandular structures are the source of milk upon lactation, and also the most common origin of breast cancer. Despite their functional and clinical importance, the three dimensional (3D) architecture of TDLUs has remained undetermined, largely due to their absence in rodent animal models. By utilizing recent technological advances in optical tissue clearing and microscopy, we imaged the 3D structure of healthy human breast tissue to determine whether general branching patterns or cell type specific niches exist in the TDLU. Our data demonstrate that TDLUs have a consistent shape and their branch parameters are largely comparable between different TDLUs and individuals irrespective of age or parity. Simulation of TDLU branching morphogenesis in 3D by mathematical modelling suggests that evolutionarily conserved mechanisms regulate mammary gland branching in humans and mice, despite their anatomical differences. The data also demonstrate a new level of organization within the TDLU structure identifying a main branch that dominates in bifurcation events and exhibits a more duct-like keratin expression pattern. In all, our data provide the first structural insights into 3D human breast anatomy and branching, and exemplify the power of volumetric imaging in deeper understanding of human breast biology.

## Introduction

Human mammary gland development and 3D structure have been described mostly based on rare tissue samples at low resolution (Russo et al., 1994; Howard and Gusterson, 2000). Initially, the mammary gland forms as an ectodermal invagination that undergoes limited branching during embryonic development, sustains isometric growth during childhood, and resumes branching morphogenesis again during puberty in response to female systemic hormones, such as growth hormone and oestrogen (Macias and Hinck, 2012). The morphology of the human breast tissue also changes dramatically during the reproductive cycles of pregnancy and lactation, as well as ageing in order to adapt to the functional requirements of the tissue.

The human mammary gland is formed of 15-20 lobes in which collecting ducts, originating from the nipple, ultimately side-branch to form TDLUs (Bannister et al., 1995) (**Fig. 1A-B**). The TDLUs, composed of an extralobular terminal duct (ETD) that branches into lobules with acini at the tips of the ducts (**Fig. 1A-B**), are considered the predominant source of breast cancer (Wellings et al., 1975; Russo and Russo, 1997; Tabár et al., 2022). Upon lactation, milk is produced by the luminal epithelium within the TDLUs, and propelled to the nursing young through oxytocin-dependent basal epithelial contractions (Gimpl and Fahrenholz, 2001; Stevenson et al., 2020). While the histology and overall anatomy of the human breast epithelium has been established and different TDLU categories defined based on donor age and parity (Russo et al., 1992), the 3D architecture of the TDLUs has remained obscure, and their illustration in the literature is quite variable. In addition, the extent to which TDLU structures vary between individuals and within a breast is unclear. Therefore, detailed understanding of the structure and composition of the TDLUs is of high clinical importance, particularly related to their key role in breast cancer.

While the human mammary gland develops into an anatomically distinct organ with lobes and TDLUs within a collagen-rich stroma (Howard and Gusterson, 2000), the mammary gland of commonly used rodent animal models is formed by a single network of branched ducts within adipose stroma (Dontu and Ince, 2015), thus redundant for studying the TDLU. Also, whether the branching mechanisms that produce the differential mammary gland outcomes are governed by the same principles in human and mouse has not been previously investigated.

Although much effort has been put into describing the mammary epithelial and stromal cell populations in the human gland by single cell analysis (Nguyen et al., 2018; Chen et al., 2022; Gray et al., 2022), it is not known how these cell types are anatomically distributed within the mammary gland. Previous studies assessing cell localisation in breast tissue sections (Dontu and Ince, 2015; Villadsen et al., 2007) or in micro-collected TDLUs/ducts (Goldhammer et al., 2022; Kohler et al., 2022) also provide limited information of the spatial distribution cell types within TDLUs. As recent advances in technology now enable the imaging of larger tissue volumes, we employed tissue clearing methods, volumetric light sheet microscopy, and mathematical modelling to describe the 3D morphology of TDLUs in the human mammary gland, and investigated whether general branching patterns or principles exist for the human TDLU.

## Results and discussion

### *Optical clearing and light sheet imaging of human breast tissue*

To image large volumes of human breast tissue, we obtained healthy or tumor-adjacent normal breast samples under informed consent from patients undergoing breast reduction or breast cancer surgery, respectively (**Fig. 1C, Table S1**). Tissue pieces of approximately 5-20 mm in diameter were pre-screened for the presence of mammary epithelium by nuclear DAPI labelling, and labelled by immunofluorescence for cytokeratin 8 (KRT8) to visualize luminal mammary epithelial cells before

optical tissue clearing (**Fig. 1C**). To avoid distortion of tissue dimensions and to allow for morphometric analysis, we first used optical tissue clearing with FUnGI protocol that, unlike several other protocols, has been reported to preserve the original size of the specimen (Almagro et al., 2021; Rios et al., 2019). With FunGI protocol, we obtained good sample transparency and were able to visualize entire TDLU structures (**Fig. 1D**). Our optimized pre-screening with nuclear labelling also allowed for targeting the TDLU structures within the tissue specimen with a large fraction of connective and adipose tissue. These results provide a workflow for clearing and volumetric imaging of human breast tissue.

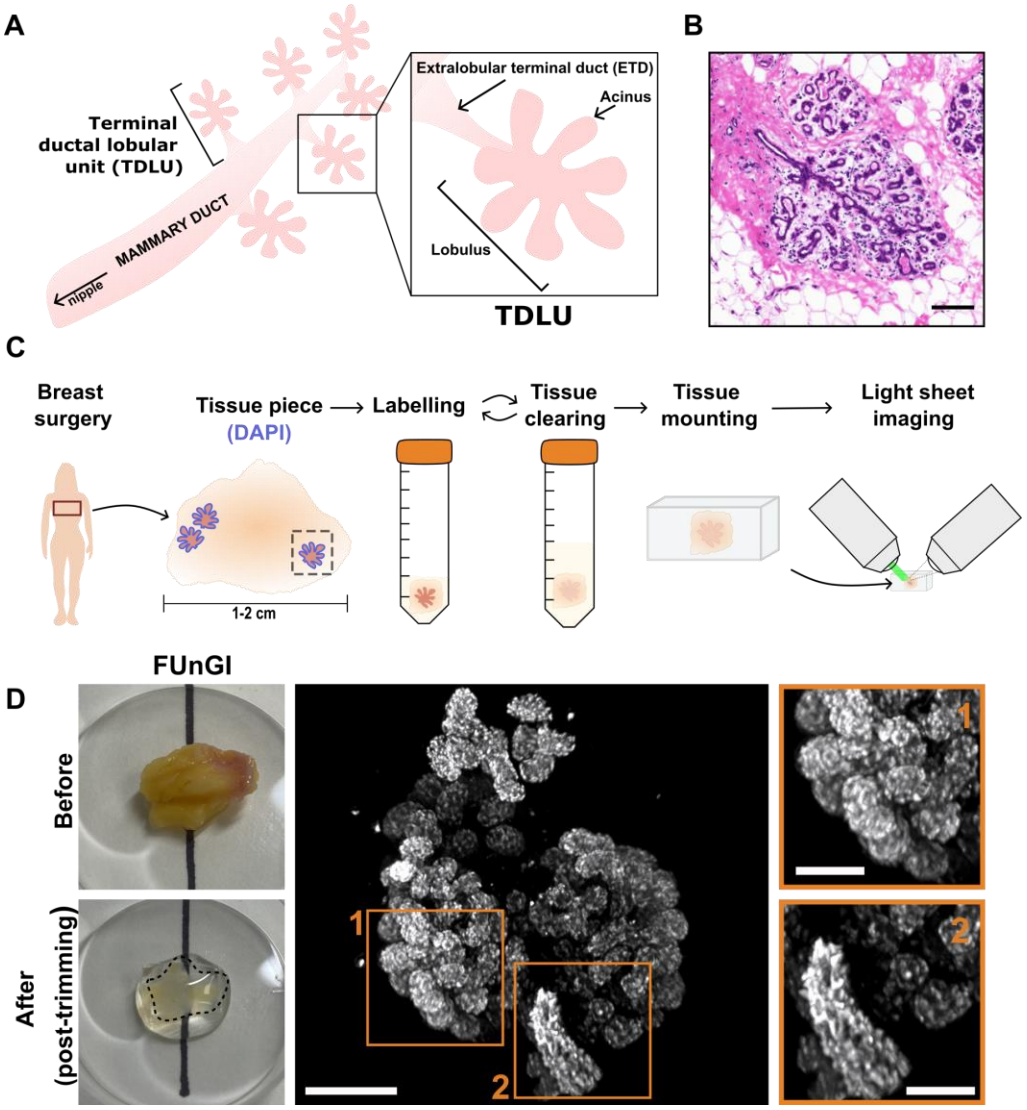


**Figure 1. Light sheet imaging of optically cleared human breast tissue.**

**A.** A schematic representation of the human breast terminal ductal lobular unit (TDLU) based on current knowledge.

**B.** An H&E stained histological section of human breast TDLU (Patient 6). Scale bar: 100µm.

**C.** Sample preparation and mounting protocol. Human breast tissue is dissected, fixed, and further trimmed to the smallest size possible utilizing DAPI signal at a fluorescence microscope. The pieces are then immunolabelled and cleared for imaging. Finally, the tissue is mounted in 2% agarose (diluted in equivalent clearing solution) to be imaged with light sheet microscopy.

**D.** Representative images of breast tissue before and after FunGI clearing (post-trimming) are shown. Sample volumes were imaged with light sheet microscopy. Magnifications are shown for two ROIs. Scale bars: 200µm (main), 100µm (ROIs).

***Branching parameters are consistent between different TDLUs and individual patients***

The morphology of entire human TDLUs has been documented with bright field or confocal microscopy imaging (Russo et al., 1992; Rios et al., 2019). In order to quantitatively establish the 3D morphology and dimensions of the human TDLU, breast tissue samples from four patients were cleared with FUnGI, and 14 TDLU structures were successfully imaged with volumetric light sheet microscopy. The donors represented different ages (range 24-50 years) and parity (range 0-2 children) (**Table S1, Fig S1**). We observed that the luminal epithelium labelled with KRT8 formed a continuous tubular structure that bifurcated in seemingly random manner and ended as enlarged acini (**Fig. 2A**), demonstrating that the imaging protocol could reveal entire TDLU structures.

For quantitative branching analysis, the 3D image stacks were segmented for KRT8 signal using WEKA trainable segmentation in ImageJ followed by quantitative analysis of the TDLU structures using Imaris FilamentTracer (**Fig. 2A, Video S1**). The results of the morphometric analysis of human breast TDLUs demonstrate regularity in branch (also referred to as ductules) length, diameter and angle (**Fig. 2C-D, Fig. 2SA-C**). The average branch length was 71 µm (s.d. 37.8 µm), diameter 35 µm (s.d. 8.9 µm), and the average branch angle with respect to the parent duct was 49° (s.d. 29.9°) (**Fig. 2D**). The TDLU tip branches (acini) were on average 1.2 times as wide in diameter as the ducts in the TDLU (**Fig. 2E**)**.** A TDLU formed most commonly from 4-6 consecutive bifurcation events, and branches at levels higher than 10 consecutive bifurcations were few (**Fig. 2F**). Average TDLU length (distance from ETD to the farthest acinus, **Fig. 2B**) and width (largest width in the direction perpendicular to the ETD direction, **Fig. 2B**) were 460 µm and 360 µm, respectively, and TDLUs typically have a regular shape with an aspect ratio of 1.5 (**Fig. 2G**). These measures are similar to the previously reported size of a normal TDLU based on HE stained tissue sections (Figueroa et al., 2014). Interestingly, the branching of normal mammary epithelium adjacent to a premalignant lesion (ductal carcinoma *in situ*) was comparable to healthy donor tissues (**Fig. 2C,** Patient 3). Our data also demonstrate that TDLUs have a consistent shape and their branch parameters are largely comparable between different TDLUs and individual patients of variable age and parity (**Fig. 2C**). In contrast to previous observations using tissue sections (Rosebrock et al., 2013), the total number of branches or acini (tips) per TDLU was not proportional to the TDLU diameter (**Fig. 2H**), suggesting that branching density may vary.

TDLUs have previously been divided into four different types of branching, where type I represents young nulliparous tissue (6-11 acini/TDLU), type II mature nulliparous tissue (12-80 acini/TDLU), type III parous tissue (>80 acini/TDLU), and type IV intense branching occurring only during pregnancy and lactation (Russo et al., 1992). Of the TDLU samples analyzed quantitatively in this study, only one contained more than 80 branches in total, thus reaching category III suggested to predominate in parous women (Russo et al., 1992). However, the donor of this sample was non-parous, and the rest of the analyzed tissues, irresepective of parity, were in the type II category (**Fig. 2H**). In addition to parity and age, menstrual cycling has been indicated to affect TDLU branching (Ramakrishnan et al., 2002). The samples analyzed here represented the follicular phase or hormonal contraception, but no differences in branch count or diameter could be linked to the hormonal status (**Table S1**). Further, the position of the TDLU within the whole gland could affect the branching type, as fibroglandular density, along with tumor incidence, has been indicated highest at the upper outer quadrant of the breast in Western women (Chen et al., 2017). Most of the samples in this study were collected from reduction mammoplasty operations, where the tissue is resected from the lower quadrants of the breast. Although the dataset analyzed here is relatively small, our data suggest that the relationship between parity and TDLU branching density may be more variable than presumed and warrants further investigation.

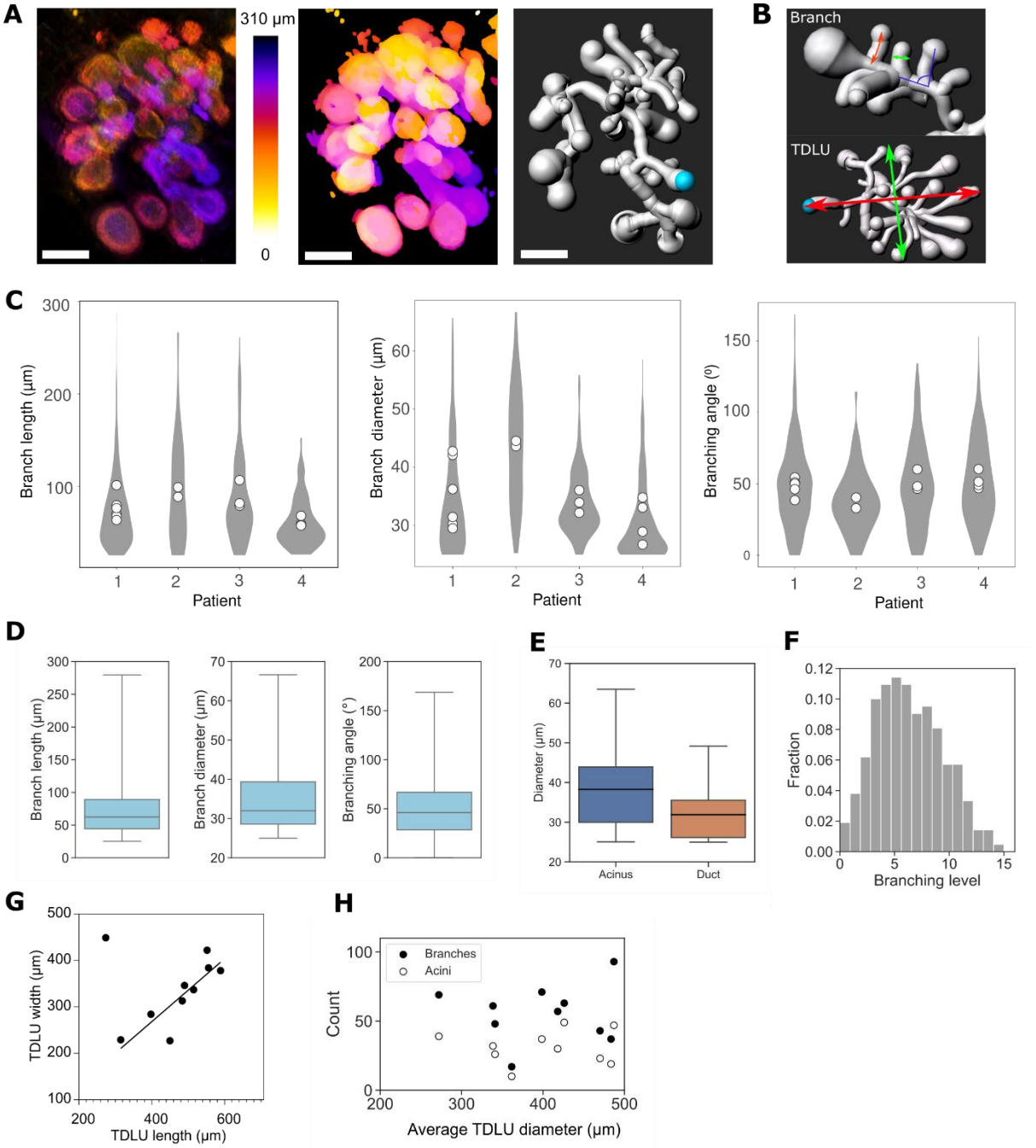


**Figure 2. Branching parameters are consistent between different TDLUs and individual patients.**
**A.** Data analysis pipeline. Image on the left shows a light sheet image of a TDLU with depth visualized using colour coding. Image in the middle shows the segmented image visualized using the same color coding. Image on the right shows branching structure model made by the Imaris FilamentTracer. Cyan dot in the image indicates the branch structure starting point. Scale bars: 100 µm.
**B.** Parameter definitions. Top image: branch length (red arrow), branch diameter (green arrow), and branching angle (blue). Bottom image: TDLU length (red arrow) and TDLU width (green arrow), cyan dot indicates the network starting point (ETD).
**C**. Distributions of the parameters branch length, branch diameter and branching angle by patient. Mean values of individual TDLUs are shown by the white dots and grey area shows value distribution.
**D.** Pooled distributions of branch length, diameter, and angle ($n_{length}$=689, $n_{diameter}$=689, $n_{angle}$=689 branches from 14 TDLUs of 4 patients). Boxes show median and interquartile range, and whiskers the full range of data points.

**E.** Distributions of acinar and ductal diameters per TDLU (n=14).
**F.** Distribution of branching levels. Data is pooled from all complete TDLU structures for which the whole network could be reliably traced (n=8 TDLUs).
**G.** Measured length and diameter of the whole TDLU. Line shows linear fit to data excluding the outlier point. TDLU aspect ratio from the fit is 1.47.
**H.** Total number of branches and tip branches (acini) in TDLU as a function of average TDLU diameter. Average TDLU diameter is the average of the measured TDLU length and width.

**Table S1. Patient sample characteristics.**

| Patient | Age (years) | Parity | Procedure | Menstrual cycle phase | Hormonal contraception | Branch length (µm) | Branch diameter (µm) | Branch angle (°) | Method | Material notes |
|---|---|---|---|---|---|---|---|---|---|---|
| *Turku University Hospital* | | | | | | | | | | |
| **1** | 24 | 0 | Reduction mammoplasty | N/A | yes | 74.1±40.4 | 34.7±9.5 | 49.9±30.6 | FUnGI | |
| **2** | 43 | 2 | Reduction mammoplasty | follicular | yes | 95.7±58.5 | 43.9±9.9 | 38.2±22.2 | FUnGI | Mastopathy |
| **3** | 50 | 0 | Mastectomy | N/A | yes | 88.8±50.5 | 34.0±5.9 | 49.6±29.9 | FUnGI | DCIS-adjacent tissue |
| **5** | 18 | 0 | Reduction mammoplasty | luteal | no | | | | iFLASH | |
| **6** | 35 | 2 | Reduction mammoplasty | luteal | no | | | | IHC | |
| **7** | 44 | 2 | Reduction mammoplasty | N/A | yes | | | | IHC | |
| **8** | 40 | 1 | Reduction mammoplasty | mid cycle | no | | | | iFLASH, IHC | |
| *Mediclinic, Belgium* | | | | | | | | | | |
| **4** | 48 | 2 | Reduction mammoplasty | follicular | no | 60.8±26.5 | 30.7±6.8 | 51.5±29.1 | FUnGI | 1.5h mild digestion |

N/A, not applicable; IHC, immunohistochemistry; DCIS, ductal carcinoma *in situ.*

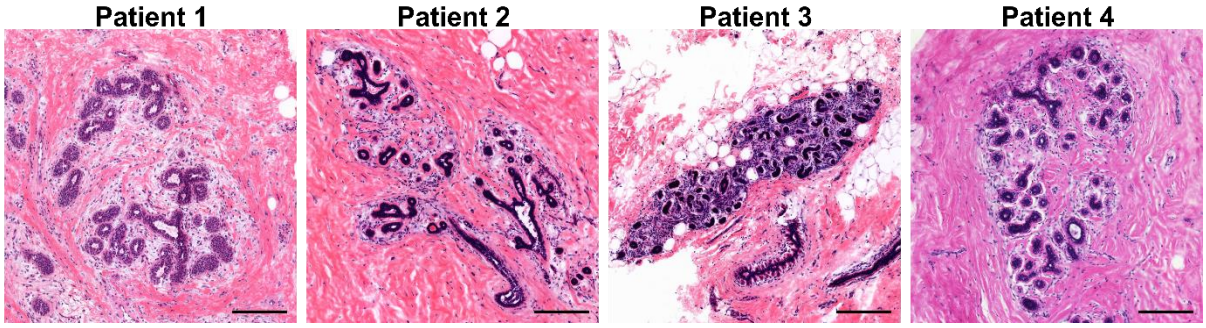


**Figure S1. Representative images of H&E-stained TDLUs in breast tissue sections of the patient samples used for quantitative branching analysis in Figure 2.** Scale bars: 100µm.

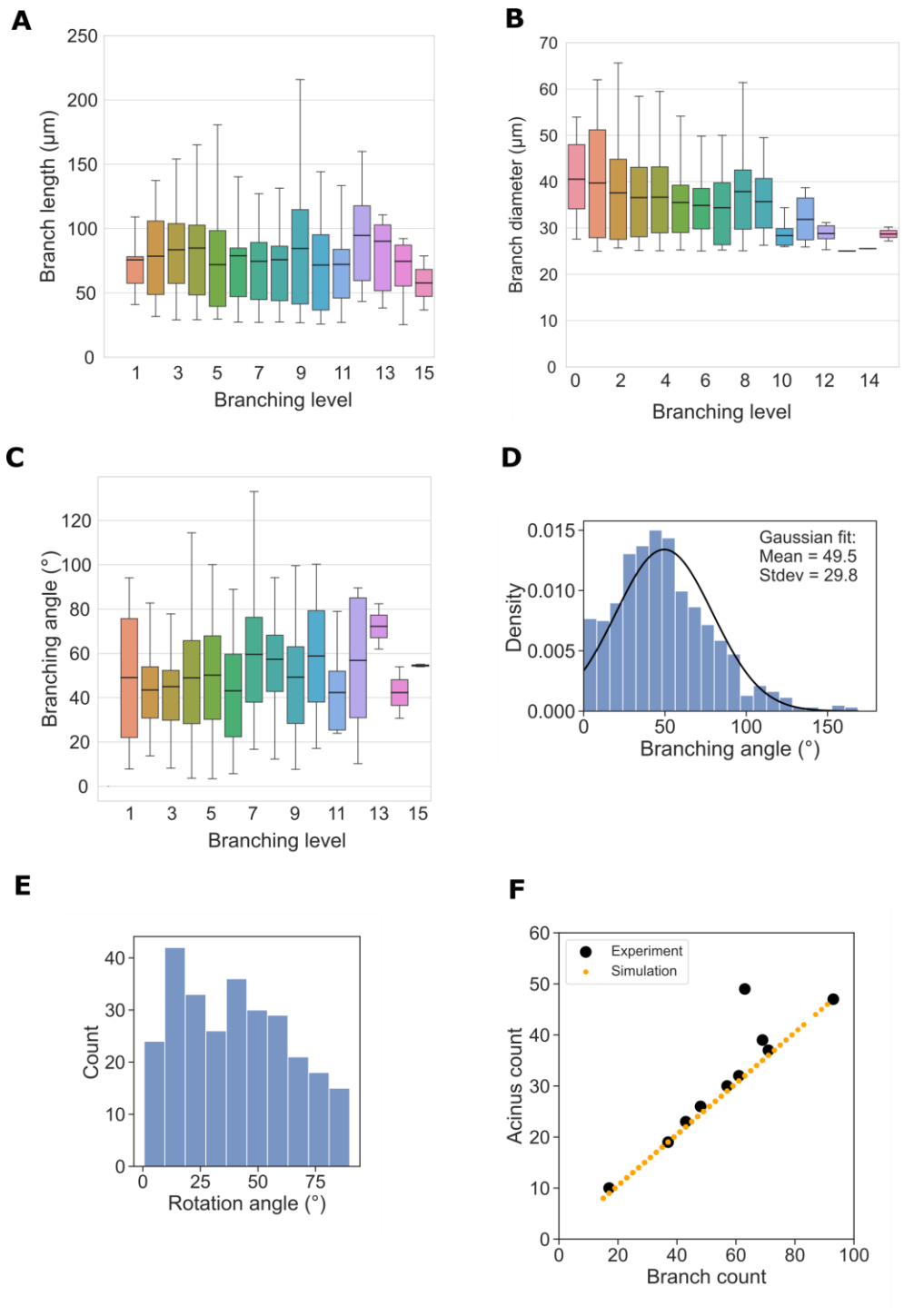


**Figure S2. Branching structure characteristics.**

**A-C.** Experimentally observed branch length (**A**), branch diameter (**B**), and branching angle (**C**) at different branching levels ($n_{length}$=670, $n_{diameter}$=670, $n_{angle}$=670 branches from 14 TDLUs of 4 patients). Boxes show median and interquartile range, and whiskers the full range of data points.

**D.** Distribution of the branching angle (branch opening angle). Fit shows the normal distribution used in simulations to draw the branching opening angles.

**E.** Distribution of the branching rotation angle. Distribution was approximated to be uniform in simulations.

**F.** Total number of branches and number of acini in a TDLU and simulated branching networks.

***Human mammary gland branching morphogenesis appears to be governed by the same principles as in mouse***

Branching morphogenesis by branching and annihilating random walk (BARW) (Hannezo et al., 2017) has been previously used to simulate generation of mouse mammary gland (Hannezo et al., 2017; Nerger et al., 2021), kidney (Hannezo et al., 2017), pancreas (Sznurkowska et al., 2018), zebrafish nervous system (Uçar et al., 2021) and cholangiocyte organoids (Roos et al., 2022). Whether human TDLUs branch and develop with the same principles as the mouse mammary gland has not been addressed. In the mouse mammary gland branching model, branches grow forward, bifurcate randomly with a constant probability, and terminate if the branch meets an existing branch or the edges of the simulation area (Hannezo et al., 2017). Furthermore, given that the mouse mammary fat pad is very flat, the simulation area was defined in 2D (Hannezo et al., 2017). For mathematical modelling of human TDLU branching, we utilized the experimentally obtained parameters for branch diameter, branching and rotation angle distributions, branching probability derived from the branch length, and TDLU volume (**Fig. 2D-E, Fig. S2D-E**, **Table S2**). Compared to mouse mammary gland, human TDLUs are smaller and 3D, which was implemented in our model.

Model geometry was parametrized using a parameter which represents the branch diameter (**Fig. 3A**). Termination distance was set equal to this branch diameter parameter to represent termination when branches touch each other (**Fig. 3A**). A branching free zone of radius equal to branch diameter parameter was established around each branching event to prevent immediate re-branching resulting in unrealistic branches that are shorter than their diameter (**Fig. 3A**). Branching probability was calculated as a fraction of simulation step size to the experimentally observed average branch length. The simulation was allowed to grow within the average volume of a TDLU observed experimentally.

Simulation with these boundaries produced ductal structures very similar to the TDLUs in human tissue samples (**Fig. 3B**). Simulated structures with less than 15 branches (5.4% of the simulations) were excluded since we could not detect such small TDLU structures in the experimental data. Branch lengths in simulated networks were comparable (**Fig. 3C**). Simulated networks tended to be smaller than those observed experimentally which is seen as lower average branch count (**Fig. 3D**) and rarer occurrence of branches in levels above generation 10 (**Fig. 3E**). Model prediction of branch level distribution followed the general trend of that observed experimentally ($R^2$ = 0.80, Fig 3E). Ratio of number of terminal branches (acini) to total number of branches in simulated branching networks is 0.51 (**Fig. S2F**) matching well the experimentally observed value 0.55. This is expected since in a bifurcating network at any given time point the number of active tips at branching level $L$ is $2^L$, and the total number of branches follows a geometric series $\sum_{i=0}^{L} 2^i = 2^{L+1} - 1$. The ratio of the number of acini to the total number of branches is then $2^L/(2^{L+1} - 1)$, which is 0.5 at large $L$. Ratios slightly higher than 0.5 seen in experimental and simulation data are explained by the terminating branches and side branching.

Topology, ancestry of the subtrees, and connectedness of the networks was compared by calculating the branch termination probability, and sizes of subtrees in levels and branch counts (**Fig. 3F, H, I**) as before (Hannezo et al., 2017; Roos et al., 2022). Probability of a branch terminating at a given level (**Fig. 3F**) follows a similar trend as observed before (Hannezo et al., 2017; Roos et al., 2022) levelling to approximately 0.5 at levels above 3. Levelling happens at earlier levels compared to e.g. mouse mammary gland due to the lower branch count in human TDLUs, which also explains the rising probability at higher levels. Simulated networks follow the trend well ($R^2$ = 0.89).

Tree plots of the branch ancestry (**Fig. 3G, Fig. S3**) show that human TDLU subtrees are not symmetric, but instead their size varies substantially within a TDLU. Many shallow subtrees are typically observed at low branch levels (spanning only 1-5 levels from the root point) and highest branching occurs in 1-2 ancestral subtree lines that continue growing up to levels 10 and above (**Fig. 3G, Fig. S3**). Comparable behaviour can also be generated by the simulations which is quantitatively shown using analysis of

subtree sizes (**Fig. 3H-I**) (Hannezo et al., 2017). The tendency of the simulated networks to be smaller than experimental is also reflected in the subtree analysis by a mismatch of model and clinical results at the higher branch levels. Overall the fit of model results to experimental observations is good $R^2$ = 0.94 for subtree persistence (**Fig. 3H**), and $R^2$ = 0.92 for subtree size in branches (**Fig. 3I**). Based on the reasoning presented for mouse mammary gland (Hannezo et al., 2017), our analysis of subtrees (**Fig. S3**) and branch parameters at different branch levels (**Fig. S2A-C**) demonstrate that the earlier fractal branching model with symmetrically occurring bifurcations, and gradually decreasing branch length and diameter (Honeth et al., 2015), does not capture the 3D branching structure of the human TDLU. Instead, a 3D simulation based on the BARW model produces a close fit suggesting that TDLU branches grow forward, bifurcate randomly with a constant probability, and terminate if the branch meets an existing branch or the edges of the TDLU area.

Considering the wide variation in the data, the simulated networks resemble highly the TDLUs in the clinical specimen, suggesting that human mammary gland branching morphogenesis is governed by the same principles as the mouse mammary gland. The most significant difference between the species in terms of the modelling parameters is the branching area which in humans was limited to a single TDLU. Why TDLUs evolved and why they adopt this particular size and shape in humans remains unknown. Furthermore, whether the morphogenesis of an entire lobe would follow comparable principles with TDLU branching remains to be studied. Specifically, it would be interesting to address, if the larger branch diameter in collecting ducts is sufficient to account for the higher branch length.

Terminated mammary ductal tips typically reside close to an existing duct or the fat pad boundary in mice (Silberstein, 2001). Additionally, ductal branching was shown to occur *in vitro* only when the tip was remote from the other ducts (Nelson et al., 2006). Consequently, ductal elongation and branching was suggested to proceed as a ‘‘default state’’ with tip termination occurring only when tips come into proximity with existing ducts or the edges of the fat pad (Hannezo et al., 2017). This scenario, as well as the modelling presented here, suggest that growth limiting mechanisms exist around the TDLUs as well. While there is currently limited information on the negative regulation of branching morphogenesis, TGFβ1 secretion (Silberstein and Daniel, 1987; Nelson et al., 2006) and progressive envelopment of the gland by extracellular matrix (Silberstein and Daniel, 1984; Osin et al., 1998) have been suggested to limit mammary gland branching. Therefore, gradual alterations in TDLU proximal stroma may contribute to TDLU growth inhibition.

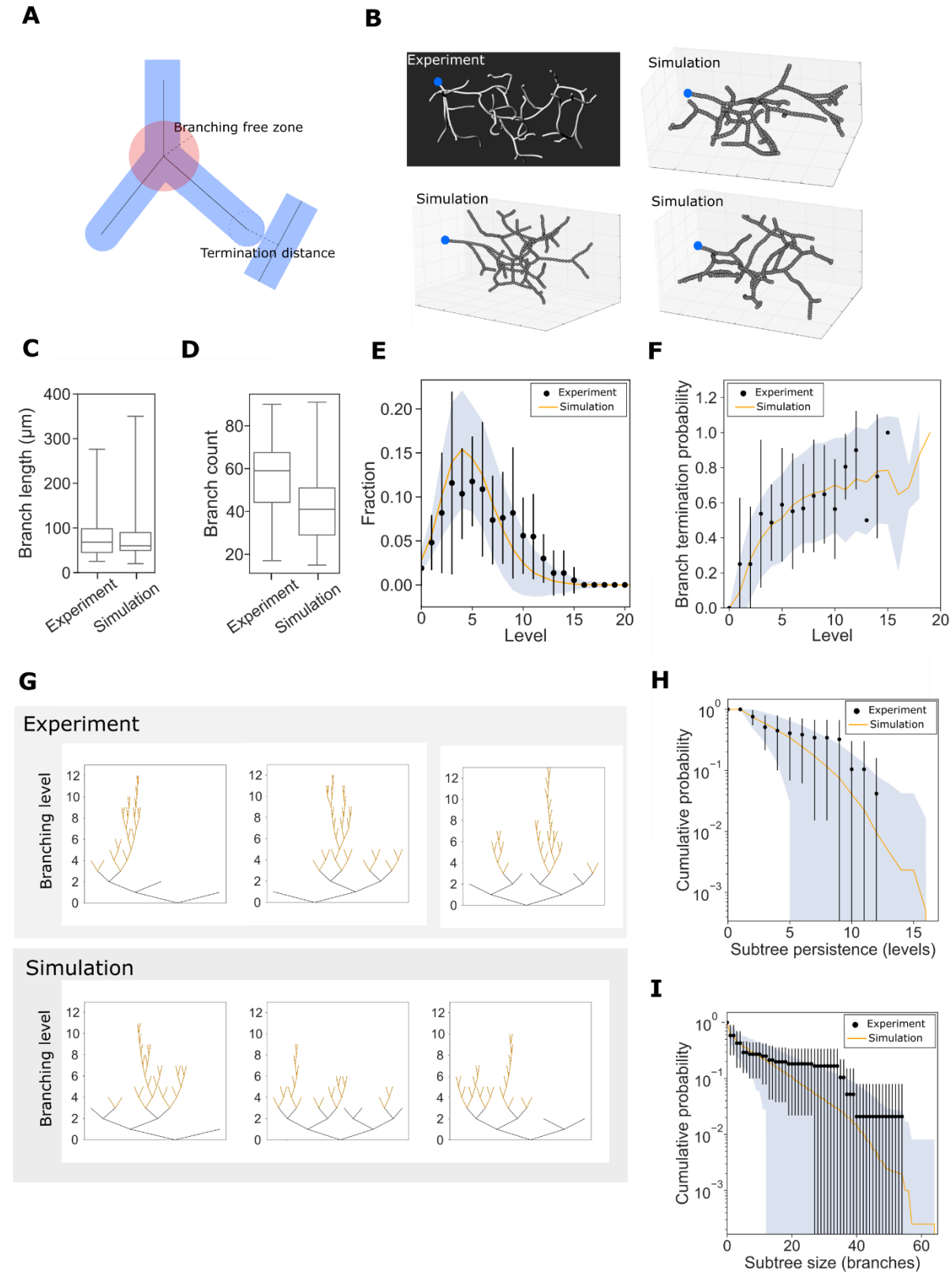


**Figure 3. Simulation of human TDLU branching morphogenesis resembles closely the experimental data.**

**A.** Schematic image drawn to scale visualizing simulation parameters branching free zone and termination distance.

**B.** Images of experimental and simulated networks. Blue dot indicates the network beginning point. Axis tics have 100 µm spacing. Plot point size is not to scale.
**C-D.** Simulation predictions for branch length (**C**) and number of branches in a TDLU (**D**) compared to experimental results.
**E.** Distribution of branching levels in experimental data and simulation results.
**F.** Probability of branch termination at different branching levels.
**G.** Examples of the ancestral connectedness of branches in experimental data and simulation results. Subtrees beginning at level 3 are shown in orange.
**H-I.** Probability of a subtree beginning at level 3 to span a number of levels (**H**) or to contain a number of branches (**I**)
In E, F, H, and I dots and error bars indicate mean and standard deviation of the experimental data, and the orange line and blue shaded area mean and standard deviation of results of 1000 simulations.
**C-I.** Data represent the results of 1000 simulation runs.

**Table S2. Comparison of the simulation branching parameters.**

| | **Branch diameter** | **Branching probability** | **Branching angle** | **Simulation volume** |
|---|---|---|---|---|
| **Human TDLU** | 40 µm | 0.15 | 49° | 460×310×310 $\mu m^3$ |
| **Mouse mammary gland** (Hannezo et al., 2017) | 3 a.u. | 0.10 | 30° | 280×150 $a.u.^2$ |

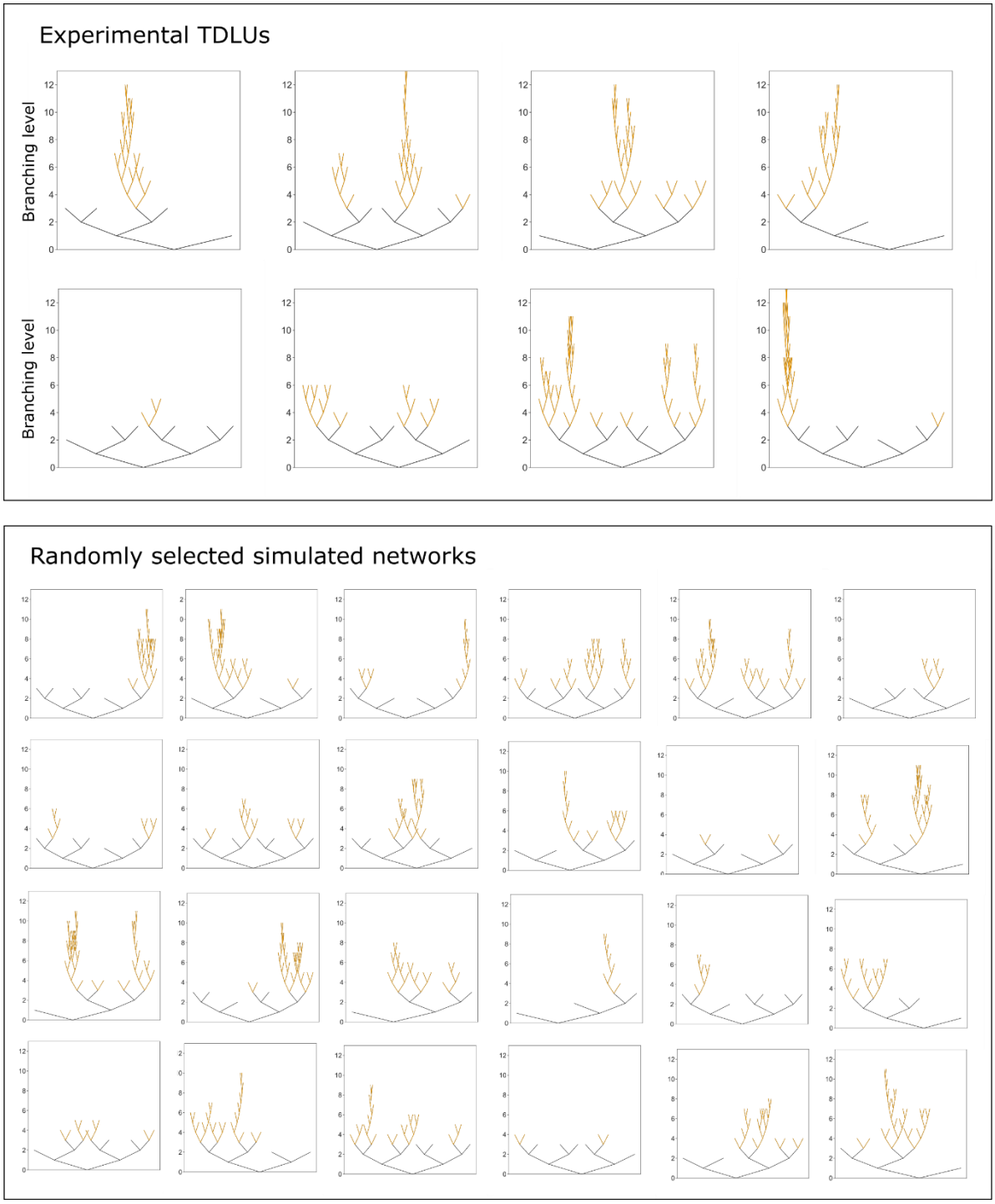


**Figure S3. Subtree graphs of all experimentally analyzed TDLUs and a subset of the simulated TDLUs.** Graphs show the full networks of experimental TDLUs and 24 randomly selected simulations.

***Volumetric imaging of TDLUs reveals spatial differences in mammary epithelial marker expression***

In addition to the 3D structure, the cellular composition and tissue organization in different parts of the TDLU remain poorly understood. Our improved version of the FLASH optical tissue clearing protocol (Messal et al., 2021) (termed hereon iFLASH) produced superior clarity compared to FunGI clearing enabling imaging with cellular resolution (**Fig. 4A**). Also, due to tissue shrinkage (Almagro et al., 2021), imaging of larger breast tissue volumes was possible with iFLASH clearing (**Fig. 4A**). KRT8 and cytokeratin 14 (KRT14) intermediate filament proteins have been established as luminal and predominantly basal epithelial markers, respectively, in the human mammary gland (Taylor-Papadimitriou et al., 1989; Gray et al., 2022). These marker proteins were first analyzed in fixed and immunolabelled healthy breast tissue sections revealing higher KRT14 expression in the basal cell layer of the ETDs compared to most parts of the lobules (**Fig. 4B**). In order to build a more comprehensive view of the KRT8/KRT14 expression within the TDLU, tissue pieces were cleared with iFLASH prior to immunolabelling and confocal (**Fig. 4C**) or light sheet microscopy imaging (**Fig. 4D-E, Video S2**). Although some KRT14 expression was detected in the entire basal mammary epithelial cell layer (**Fig. 4C-D**), a subpopulation of basal cells expressing a high level of KRT14 ($KRT14^{hi}$) was detected predominantly in the ETDs of whole TDLUs (**Fig. 4C-E**), as expected based on the tissue section analysis (**Fig. 4B**). However, volumetric imaging revealed that the $KRT14^{hi}$ basal cells present in the lobules reduce gradually from ETD towards the acini (**Fig. 4D-E**), and the main subtree of a TDLU retains a higher number of $KRT14^{hi}$ basal cells (**Fig. 4F, Fig. S4**). Conversely, the expression of the luminal marker KRT8 appeared to increase in intensity towards the acini (**Fig. 4B-D**). These data demonstrate a new level of organization within the TDLU structure identifying a main branch that dominates in bifurcation events and exhibits a more duct-like KRT14 expression pattern.

Myoepithelial cell markers, including KRT14, are commonly used to distinguish invasive breast carcinomas from precancerous lesions but the evident heterogeneity in their expression patterns in healthy breast epithelium and different stages of breast tumors remains poorly understood (Gusterson et al., 2005; Hilson et al., 2009; Russell et al., 2015). KRT14 has previously been linked to increased adhesive and migratory properties (Fujiwara et al., 2020; Cheung et al., 2013), as well as mechanical integrity of cells (Ramms et al., 2013). The gradual decline in $KRT14^{hi}$ cells towards the acini of the TDLU could, therefore, reflect the distinct requirements that the functional domains of the organ impose on the mechanical properties of the basal mammary epithelium. In all, these data demonstrate that optical clearing with iFLASH and volumetric imaging of entire TDLUs can be used for studying the relationship between TDLU architecture and the cell types that form it.

Overall, this study presents the first systematic analysis and mathematical modelling of the glandular 3D structure in normal human breast epithelium. Our findings add a new layer of detail on the anatomy of the human breast. This study also provides a protocol and framework for future investigations on the role of ductal architecture in the regulation of growth in healthy and malignant breast epithelium, including carcinogenesis and invasive progression. Importantly, the identities and niches of distinct cell types within the TDLU structure are likely to become clearer as research proceeds, revealing previously unknown structure-function relationships in the breast tissue.

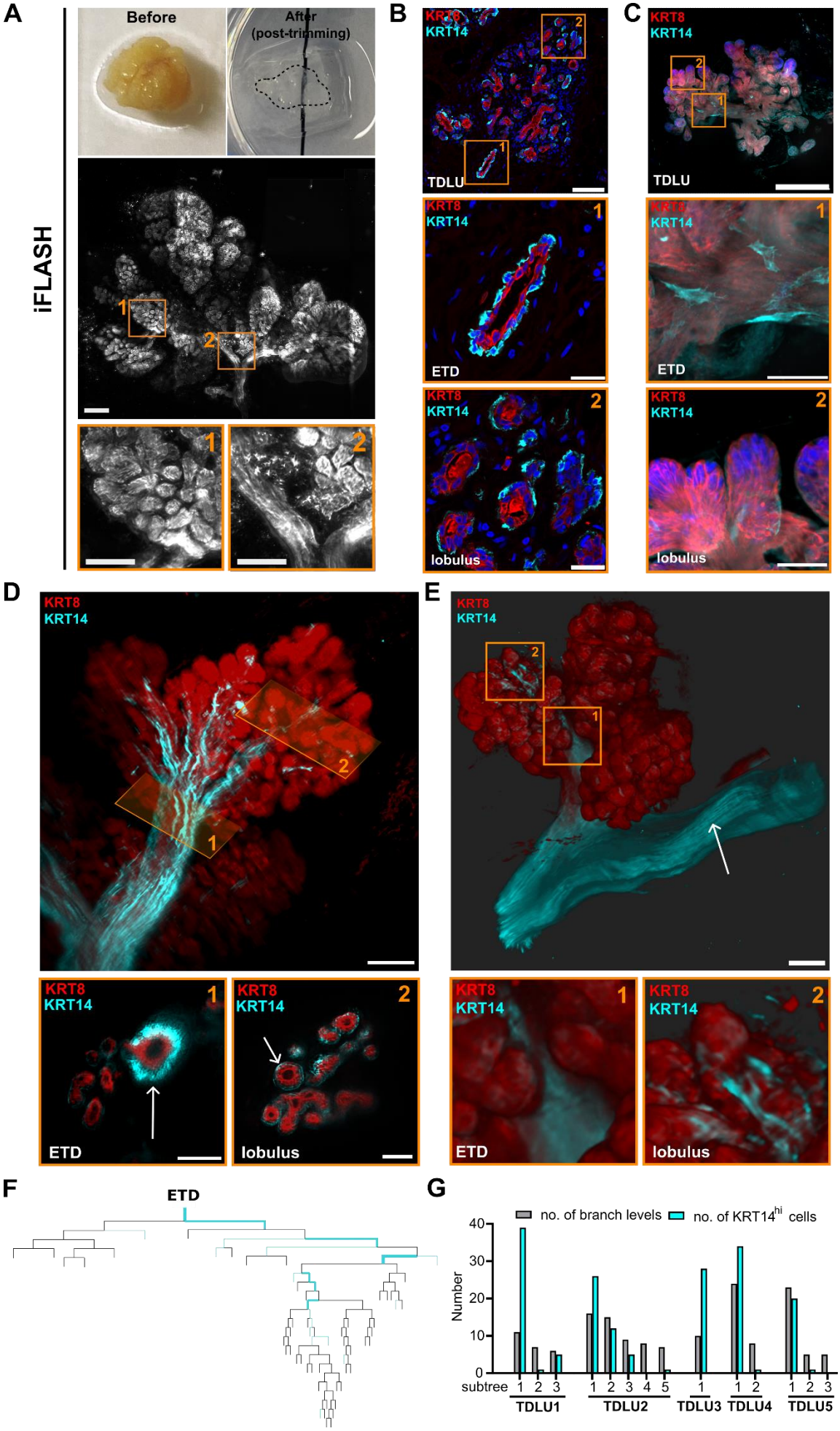
A
Before
After
(post-trimming)
iFLASH
B
KRT8
KRT14
TDLU
ETD
lobulus
C
KRT8
KRT14
TDLU
ETD
lobulus
D
KRT8
KRT14
ETD
lobulus
E
KRT8
KRT14
ETD
lobulus
F
ETD
G
no. of branch levels
no. of KRT14hi cells
Number
subtree
TDLU1
TDLU2
TDLU3
TDLU4
TDLU5

**Figure 4. Imaging of entire TDLUs reveals spatial differences in keratin expression patterns.**

**A.** Representative images of breast tissue before and after (post-trimming) iFLASH clearing are shown. Sample volumes were imaged with light sheet microscopy. Magnifications are shown for two ROIs. Scale bars: 200µm (main), 100µm (ROIs).

**B-C.** Confocal microscopy imaging of KRT14 (basal epithelial, cyan), KRT8 (luminal epithelial, red) and nuclei (blue) in immunolabelled frozen human breast tissue sections (**B**) or in entire TDLUs of cleared breast tissue pieces (**C**). Higher levels of KRT14 are detected in the extralobular terminal duct (ETD) compared to the lobules of TDLUs. Scale bars (A): 100 µm (main), 25 µm (ROIs), (B): 250 µm (main), 50 µm (ROIs). Images are representative of 17 TDLUs from 3 patient samples (A) and 9 TDLUs from 2 patient samples (B).

**D-E.** Light sheet microscopy imaging of KRT14 (basal epithelial, cyan) and KRT8 (luminal epithelial, red) in entire TDLUs within cleared breast tissue pieces (**D**). KRT14$^{hi}$ cells are visible in the duct (arrow), ETDs (ROI 1) and lobuli (ROI 2). Lower level of KRT14 is detected in the rest of the basal mammary epithelium (**E**). Scale bars: 100µm (main), 50µm (ROIs). Images are representative of 20 TDLUs from 2 patient samples.

**F.** Tree structure of a TDLU with the distribution of KRT14$^{hi}$ cells within the branching hierarchy (TDLU 5, cyan; line width is representative of number of KRT14$^{hi}$ cells in each branch. Branch length not to scale.)

**G**. Quantification of the branch levels and KRT14$^{hi}$ cells in individual subtrees of the TDLUs demonstrating that the dominant subtrees retain high KRT14 level (n=5, from 1 patient sample). Separate subtrees defined to begin at branch level = 3 and to contain at least 5 levels in total.

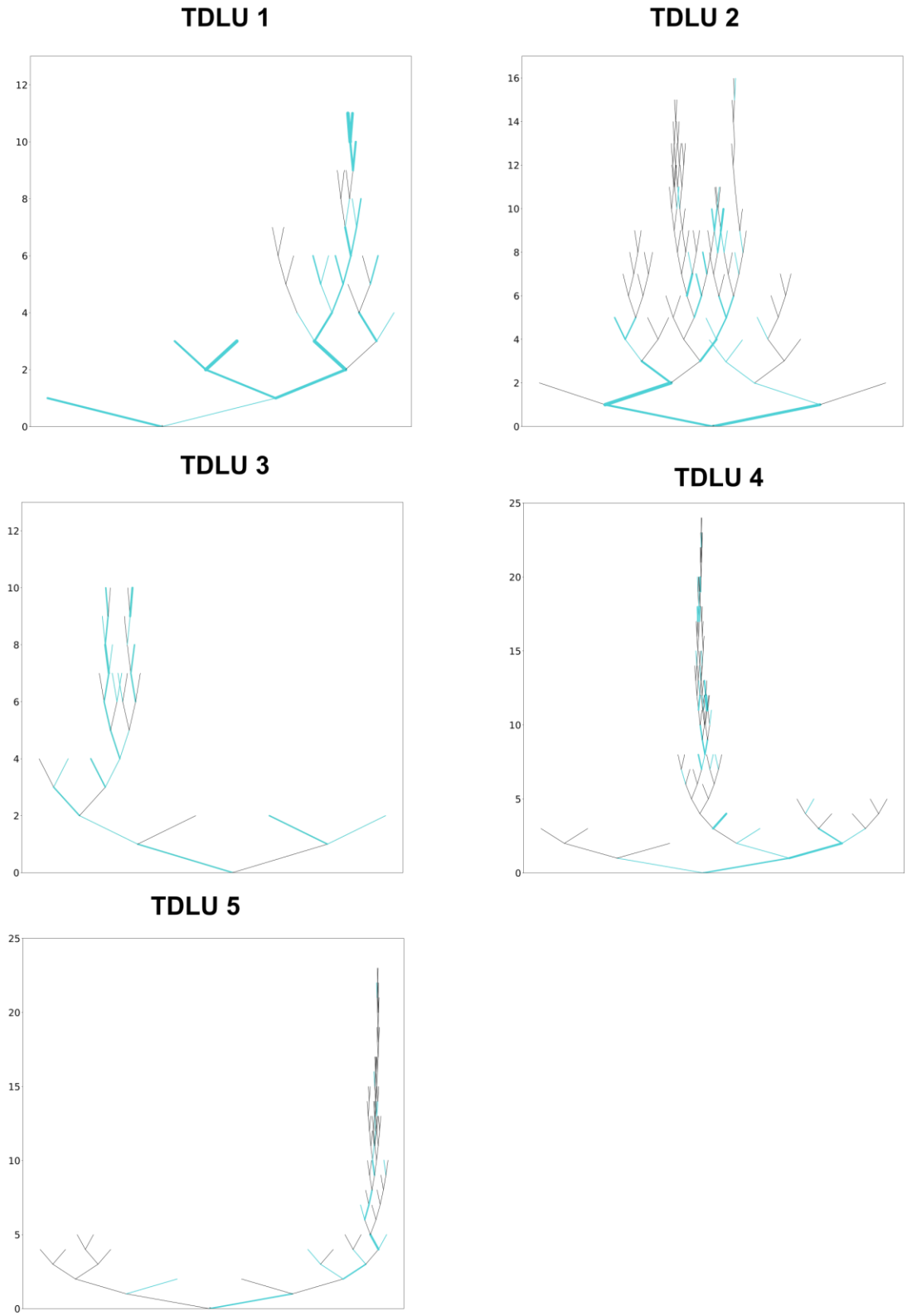


**Figure S4. Subtree structures with quantification of KRT14$^{hi}$ cells.** Tree structure of 5 TDLUs with the distribution of KRT14$^{hi}$ cells within the branching hierarchy (cyan; line width is representative of number of KRT14$^{hi}$ cells in each branch. Branch length not to scale.)

## Materials and methods

### *Human breast tissue*

At the Turku University Hospital, normal breast tissue was obtained from patients undergoing breast reduction mammoplasty. Normal breast tissue adjacent to the tumor was collected in mastectomy due to pre-invasive carcinoma. Tissues were voluntarily donated upon written informed consent at Turku University Hospital (Ethical approval ETKM 23/2018), and the donors filled a questionnaire providing details of the reproductive history and hormonal medication. At Mediclinic in Oud-Heverlee (BE), human breast tissues were anonymously retrieved from healthy donors who underwent voluntary cosmetic reduction surgery in the absence of any medical indication. All donors were adequately informed by third party clinicians about the use of the tissue and provided written informed consent for the use of the resection material and publication of the experimental results. Limited and fully anonymous donor information (age, parity status, familial cancer risk) was obtained without any link to the donor's medical record. All tissues were surgically dissected to obtain pieces with glandular tissue, and processed for fixation. For samples with high apparent mammographic density, a mild pre-digestion in collagenase was utilized before fixation (1.5h with 300 U/ml collagenase [Sigma, C7657]).

### *FUnGI clearing*

Tissue clearing and immunolabelling of tissue pieces was done following previously described FunGI protocol (Rios et al., 2019). All incubation steps were performed on a roller mixer. Tissue pieces were fixed in 4% PFA in +4°C for 24 h, and stored in PBS + 1:100 penicillin/streptomycin at +4°C until labelling. Fixed tissue pieces were labelled with DAPI (1:1000-1:3000) in PBS for 2 days in +4°C. The areas with TDLU structures were visualized with fluorescence microscopy, and chosen areas cut into pieces of approximately 3-5 mm in diameter. Tissues were washed in wash buffer (WB; 50 µg/ml ascorbic acid [Sigma, A4544], 0.05 µg/ml L-glutathione [Alfa Aesar, J62166] in PBS + 0.1% Tween) for 30 min, and in WB1 (50 µg/ml ascorbic acid , 0.05 µg/ml L-glutathione in PBS + 0.2% Tween + 0.2% Triton X-100 [Sigma, T8787] + 0.2% SDS [Amresco, 0227] + 0.2% BSA [Biowest, P6154]) for 2-3 hours in +4°C, and incubated in anti-keratin 8 primary antibody (1:100 [Hybridoma Bank, TROMA-1]) diluted in WB2 (50 µg/ml ascorbic acid, 0.05 µg/ml L-glutathione in PBS + 0.1 % Triton X-100 + 0.02% SDS + 0.2% BSA) for 2 days in +4°C. After, pieces were washed 3x1 h in WB2, and incubated in anti-rat secondary antibody (1:400 [Thermo Fisher Scientific, Alexa Fluor 594]) diluted in WB2 for 36 h. Pieces were the washed again 3x1 h in WB2, after which they were moved to ~25-30 ml of freshly prepared FUnGI solution (FUnGI base: 50% glycerol [Honeywell, 15675690], 2.5 M fructose [ACROS Organics, 1064642], 2.5 M urea [ACROS organics, 424585000], 10.6 mM Tris Base, 1 mM EDTA. Prior to clearing, add: 50 µg/ml ascorbic acid, 0.05 µg/ml L-glutathione) and incubated for 2 hours in room temperature. Finally, pieces were moved to ~25-30 ml of fresh FunGI solution and incubated at minimum o/n in +4°C, or until mounting.

### *iFLASH clearing*

Tissue clearing and immunolabelling were adapted from previously described protocol (Messal et al., 2021). All incubation steps were performed on a roller mixer. Tissue pieces were fixed with 4% PFA in SDS permeabilization buffer (10% SDS in $H_2O$, pH 7.4) o/n in +4°C. The next day, pieces were washed 3x5 min with PBS and moved to SDS permeabilization buffer for 1-2 days in +37°C. Fixed tissue pieces were then transferred to 25-50ml of CUBIC 1 (1.6 M urea, 5% Quadrol [Sigma, 122262], 15% Triton X-100, 25 mM NaCL [Fisher Scientific, S/3160/60] in $ddH_2O$) (Susaki et al., 2014) and incubated in +37°C for a minimum of 3 weeks, changing the buffer every 2-3 days. Next, the pieces were labelled with DAPI (1:1000-1:3000, [Life Technologies, D1306]) in PBS o/n at room temperature. The areas with TDLU structures were visualized with fluorescence microscopy, and chosen areas cut into pieces of approximately 2-5mm in diameter. Tissues were then permeabilized again using SDS permeabilization

buffer for 2 days in +37°C, changing the buffer between the days. The tissues were then washed 3x1h in PBT at room temperature (PBS + 0.2% Triton X-100, pH 7.4) and blocked with iFLASH blocking buffer (10% FBS [Sigma, 122262], 5% DMSO [Chem Cruz, 358801], 0.1% $NaN_3$, 1% BSA in PBT) for 1h at room temperature, and incubated in primary antibodies diluted in iFLASH blocking buffer for 3 days (anti-keratin 8 primary antibody 1:100 [Hybridoma Bank, TROMA-1]; anti-keratin 14 primary antibody 1:100 [Biolegend, 905301]). Tissues were washed 3x1h with PBT at room temperature, and pieces incubated in secondary antibodies (anti-rat secondary antibody (H+L) 1:400 [Thermo Scientific, Alexa Fluor 488], anti-rabbit 568 secondary antibody (H+L) 1:400 [Thermo Scientific, Alexa Fluor 568]) in +37°C. Finally, the pieces were washed 3x1h with PBT at room temperature, and transferred to 25-50ml of CUBIC2 (1.2 M sucrose [Millipore, 107651], 3.6M urea, 9% triethanolamine [Sigma, 90279], 0.1% Triton X-100 in $ddH_2O$) (Susaki et al., 2014) for a minimum of 2 days in +37°C, or until mounting and imaging.

***Tissue sample and bead mounting***

Labelled and cleared tissue pieces were imaged again to trim and position them optimally for the light sheet imaging excitation and emission light paths. Pieces were mounted in 3.5 mm dishes in 2% agarose [Lonza, 50180] diluted in milliQ water (FunGI protocol) or CUBIC2 (iFLASH protocol), and let set at +4°C. The solidified agarose blocks were cut out and trimmed to approximately 8 mm in diameter to fit available imaging set up. Blocks were transferred to 25-30 ml fresh FunGI or CUBIC2 respectively and incubated at minimum o/n in +4°C, or until imaging.

For deconvolution, bead samples were prepared for point spread functions. Beads [Fluoro-max Fluorecent Polymer Microspheres, Thermo Scientific] were diluted 1:10 000 - 1:20 000 in 2% agarose (as described previously) and vortexed well for uniform distribution. Mixture was let settle for 10 minutes at room temperature to allow bubbles to rise to the surface, and then mounted into an Eppendorf lid. The solidified pieces were then cut out. Additionally for FunGI protocol, bead samples were incubated in FunGI o/n before imaging.

***Immunohistochemistry of frozen tissue sections***

Tissue samples were fixed overnight at +4°C in periodate–lysine–paraformaldehyde (PLP) buffer (1% paraformaldehyde [Thermo Scientific, 28908], 0.01M sodium periodate [Sigma, 311448], 0.075 M L-lysine [Alfa Aesar, 15404639] and 0.0375 M P-buffer [0.081 M Na2HPO4 and 0.019M NaH2PO4; pH 7.4]). After washing twice with P-buffer, samples were incubated in 30% sucrose in P-buffer for a minimum of two days. Samples were mounted in Tissue-Tek® O.C.T. Compound [Sakura, 4583] on dry ice and cut into 8 µm sections.

For immunofluorescence labelling, the frozen sections were first thawed for 1 h at room temperature. The sections were blocked and permeabilized in permeabilization buffer (2% BSA, 0.1% Triton X-100 in PBS) for 30 min at room temperature. Primary antibodies were incubated in 2% BSA in PBS overnight at +4°C (anti-keratin 8 primary antibody 1:1000 [Hybridoma Bank, TROMA-1]; anti-keratin 14 primary antibody 1:1000 [Biolegend, 905301]). Then, the sections were washed 3 x 10 min with PBS and incubated with the secondary antibodies, diluted in 2% BSA in PBS, for 1 h at room temperature (anti-rabbit secondary antibody (H+L) 1:400 [Thermo Scientific, Alexa Fluor 488], anti-rat 568 secondary antibody (H+L) 1:400 [Thermo Scientific, Alexa Fluor 568]). Sections were then washed 3 x 10 min with PBS (1:1000 DAPI in the second wash) and then 5 min with milliQ water. Finally, the sections were mounted under a #1.5 glass coverslip with Mowiol® [Calbiochem] supplemented with 2.5% 1,4-diazabicyclo[2.2.2]octane [DABCO, Sigma-Aldrich].

***Light sheet microscopy and deconvolution***

Samples were imaged with MSquared Aurora Airy Beam Light Sheet microscope using Aurora acquisition software version 0.5. The objective used was a Special Optics dipping objective which has dipping medium refractive index (RI) dependent magnification 15.3×-17.9× (NA 0.37-0.43) in

immersion medium refractive index range 1.33-1.56. Alexa488 secondary antibody was imaged with a 488 nm laser and emission filter at 500-540 nm and Alexa594/Alexa568 secondary antibodies with a 568 nm laser with long pass emission filter at 570 nm. 3D images were acquired by taking z-stacks with 400 nm spacing with a pixel size of 387 nm. Images were deconvoluted using Aurora Deconvolution software version 0.5 using point spread functions of fluorescent beads obtained from agarose embedded samples.

***Confocal imaging***

Cleared tissue samples were placed in 3.5mm glass-bottom dishes [Cellvis, D35-14-1-N] for imaging, additionally under a #1.5 coverslip covered in Vectashield [Bionordika, H-1000-10] if necessary to reach maximum imaging depth. Samples were imaged with the 3i Marianas CSU-W1 spinning disk (50µm pinholes) confocal microscope using SlideBook 6 software. The objective used was a 10x Zeiss Plan-Apochromat objective (NA 0.45). Signal was detected with the following solid-state lasers and emission filters; 405nm laser, 445/45nm; 488nm laser, 525/30nm; 561nm laser, 617/73nm. 3D images were acquired by taking z-stacks with a 2µm step size using a Photometrics Prime BSI sCMOS camera with a pixel size of 6.5 µm. Images were 16bit with pixel dimensions 2048×2048.

Tissue sections labelled with immunofluorescence were imaged at the same setup using the 20x Zeiss Plan-Apochromat (NA 0.8) and 63x Zeiss Plan-Apochromat (NA 1.4) objectives. Images were acquired by taking a z-stack with 6 slices with the step size of 1 µm.

***Image segmentation and branching analysis***

Only images reliably showing a substantial fraction of the TDLU volume were chosen for images analysis (n=14). Segmentation of the 3D image was done using the Trainable WEKA Segmentation plugin (Arganda-Carreras et al., 2017). Images were preprocessed with background subtraction by rolling ball algorithm. A random forest pixel classifier was trained individually to each 3D image. 3-5 of the images in each image stack were used as training data, and a 200 tree and 2 feature random forest classifier was trained using Gaussian blur, mean, maximum, minimum, median, Laplacian, entropy, Sobel, difference of Gaussians, bilateral and Kuwahara filters as features. Segmentations were manually checked and fixed for mistakes.

Quantitative analysis of the segmented TDLU structures was done by FilamentTracer function of Imaris 8.1.2 (Bitplane ltd.). After automatic placement of seed points using a minimum size of 25 µm estimated from the minimum branch diameter in the data, seed points were manually checked and edited when necessary. Model surface was manually thresholded to match the surface of the TDLU branches in the data. Branch diameters were calculated as the shortest distance from the distance map. Resulting filament models were extensively manually checked for errors and corrected before quantitative measurements were exported. Of all the analyzed TDLUs only the ones showing the whole TDLU volume, and in which the connectedness of the branches could be reliably traced were selected for analyses concerning topological properties of the whole TDLU (n=8). Filament models of those 8 TDLU structures were exported as TIFF stacks from Imaris and further analyzed using Tree Surveyor version 1.0.12.1 (Short et al., 2013) to extract parameters of subtree ancestry, network connectedness and the branching rotation angles. Rotation angles where extracted as the sharp (0-90$^{o}$) angle between two planes defined by branches in two successive branching events.

Localization of KRT14$^{hi}$ cells was observed from analyzed filament models in Imaris, and matched to corresponding subtree ancestry and network connectedness in Tree Surveyor.

***Mathematical modelling***

BARW simulations were implemented as in (Hannezo et al., 2017). 1000 simulations were run to generated the dataset. At each simulation step each active branch can do one of three possibilities:

(1) it can grow by one more step, (2) it can branch to two child branches or (3) it can terminate (i.e. stop growing and become inactive) if it meets an existing branch or limits of the simulation volume. Each branch has a propagation direction unit vector $\widehat{\boldsymbol{k}}(t)$ pointing to the direction of branch growth at time $t$. At each simulation step a random number in [0,1] is drawn and branching happens if the number is smaller than the branching probability. Otherwise the branch grows forward one step in direction $\widehat{\boldsymbol{k}}$. Similar to (Hannezo et al., 2017), at each step the branching angle is diffused by a random angle in range [0, 15°] (angle range determined as in (Roos et al., 2022)) and a rotation angle in range [0, 360°] to prevent unnatural line-straight branches. If branching happens, two branching angles $\beta$ are drawn from a Gaussian distribution fitted to experimental branching angle distribution (**Fig. S2E**), and two angles $\theta$ are drawn from a uniform angle distribution of [0, 360°] to represent the rotational directions of the new branches around the parent branch (**Fig. S2F**). An active branch terminates if its tip gets within termination distance $r_T$ from an existing branch network point. Simulation starts with one active tip starting to grow with $\widehat{\boldsymbol{k}} = \widehat{\boldsymbol{e}}_{\boldsymbol{x}}$. Simulation runs until there are no active tips left.

3D vector rotations are done by the Rodrigues' vector rotation (Vince, 2021).

$$\boldsymbol{v_{rot}} = \boldsymbol{v}\cos\alpha + (\widehat{\boldsymbol{a}} \times \boldsymbol{v})\sin\alpha + \widehat{\boldsymbol{a}}(\widehat{\boldsymbol{a}} \cdot \boldsymbol{v})(1 - \cos\alpha) \qquad (1)$$

where $\boldsymbol{v}$ is the original vector to be rotated by angle $\alpha$ around the axis defined by the unit vector $\widehat{\boldsymbol{a}}$, and $\boldsymbol{v_{rot}}$ is the final rotated vector.

Direction vectors $\widehat{\boldsymbol{k}}$ of the new branches in 3D space are calculated using the following algorithm: first a reference unit vector defining a direction perpendicular to parent branch direction is calculated as $\widehat{\boldsymbol{u}} = \widehat{\boldsymbol{k}} \times \widehat{\boldsymbol{e}}_{\boldsymbol{y}}$, where $\widehat{\boldsymbol{e}}_{\boldsymbol{y}}$ is the standard unit vector along *y*-axis. Vector $\widehat{\boldsymbol{u}}$ is then rotated by the rotation angle $\theta$ around parent branch's $\widehat{\boldsymbol{k}}$ vector using Eq. (1) to get a randomly in [0,360°] oriented rotation axis $\widehat{\boldsymbol{a}}$ for the final rotation with the branching angle $\beta$. The direction of the child branch is then calculated by rotating the parent branch's direction vector $\widehat{\boldsymbol{k}}$ by branching angle $\beta$ around the axis $\widehat{\boldsymbol{a}}$ again using Eq. (1).

Branch diameter was used as general parameter to govern certain aspects of simulation behaviour instead of using many simulation parameters for which values would be hard to extract from experimental data. Termination distance was set equal to the branch diameter parameter describing a contact between the two branches (**Fig. 3A**). To prevent immediate termination by the parent and sibling branch at the branching event, termination events only in the front half-space of the active tip were taken into account like in (Roos et al., 2022). As observed previously (Roos et al., 2022), simulation produces realistic networks only if immediate re-branching after a branching event is prevented. We set the radius of this branching free zone (**Fig. 3A**) equal to the branch diameter parameter, which sets a requirement that branches shorter than their width are not mature enough to branch again. Branch diameter parameter value of 40 µm was used in the simulations. It was estimated by adding an extra 5 µm for the basal cell layer to the experimentally observed 35 µm branch diameter of the luminal cell layer. Branching probability was estimated to be 0.15 by comparing the experimentally observed average branch length 71.3 µm to the used simulation step of 10 µm. Simulation parameters were scaled to represent units of µm.

Simulation volume was not confined to a predetermined box, but the network was allowed to grow in the direction it chooses. Simulation volume was controlled by terminating any branch that wanders further in length from the origin (maximum length) or wider from the general direction of the network (maximum width) than allowed by the limits. General direction of the network was determined as a vector from origin to centroid of the set of current network points. Maximum length was set equal to experimentally observed average TDLU length of 460 µm and maximum width to 310 µm to create limiting volume of typical TDLU size and having aspect ratio of 1.5

Coefficient of determination $R^2$ was used to quantify the goodness of the model predictions $R^2 = 1 - \frac{\sum_{i=0}^{n}(y_{obs}^{i} - y_{model}^{i})^2}{\sum_{i=0}^{n}(y_{obs}^{i} - \bar{y})^2}$, where $y_{obs}^{i}$ and $y_{model}^{i}$ are the experimentally observed value and model prediction of data point $i$, and the average value of the observation calculated as $\bar{y} = (1/n)\sum_{i=0}^{n} y_{obs}^{i}$ (Hannezo et al., 2017).

**Code availability**

The mathematical model used for 3D simulation of TDLU branching is available on Mendeley Data (Peurla, 2023).

**Acknowledgments**

We thank the patients that voluntarily donated their tissue to this study, the clinical staff of Turku University Hospital and Mediclinic, Oud-Heverlee (BE) for assisting in sample collection, Minna Santanen for technical assistance, and all the lab members for constructive feedback over the course of this project. The Cell Imaging and Cytometry Core facility (Turku Bioscience, University of Turku, Åbo Akademi University, and Biocenter Finland), Histocore (Institute of Biomedicine, University of Turku), and Turku Bioimaging are acknowledged for services, instrumentation and expert advice. This work was supported by Sigrid Jusélius Foundation, Academy of Finland research fellowship (323096), and the Hospital District of Southwest Finland (11083). OP has been supported by Turku Doctoral Program of Molecular Medicine.

**Author contributions**

Conceptualization: MP, OP, EP; methodology: MP, OP, LM, CS, EP; formal analysis: MP, OP; investigation: MP, OP, ET, SS, LM, NB, PB, PH; writing—original draft: MP, OP, EP; writing—review and editing, all authors; visualization: MP, OP; supervision: CS, PH, EP; funding acquisition: CS, EP

**Declaration of interests**

The authors declare no competing interests.

**Supplemental information**

**Figure S1.** Representative images of HE-stained tissue sections of the patient samples used for quantitative branching analysis in Figure 2.

**Figure S2.** Branching structure characteristics.

**Figure S3.** Subtree graphs for all experimentally analyzed TDLUs and a subset of the simulated TDLUs.

**Figure S4.** Subtree structures with quantification of KRT14$^{hi}$ cells.

**Table S1.** Patient sample characteristics.

**Table S2.** Comparison of the simulation branching parameters.

**Video S1. TDLU 3D branched structure is revealed through the analysis of KRT8 signal.** Image volume sequence and Imaris filament tracer analysis of two adjacent TDLUs. KRT8 (red). Scale bar length shown (varies).

**Video S2. Visualization of iFLASH-cleared TDLU-structures reveals that k14$^{hi}$cells localise mainly along the main subtree of the TDLU.** Image volume sequence, Imaris filament tracer analysis and surface rendering of a KRT14 (cyan) /KRT8 (red) labelled TDLU. Scale bar length shown (varies).

## References


Almagro, J., H.A. Messal, M. Zaw Thin, J. van Rheenen, and A. Behrens. 2021. Tissue clearing to examine tumour complexity in three dimensions. *Nat Rev Cancer*. 21:718–730. doi:10.1038/s41568-021-00382-w.

Arganda-Carreras, I., V. Kaynig, C. Rueden, K.W. Eliceiri, J. Schindelin, A. Cardona, and H. Sebastian Seung. 2017. Trainable Weka Segmentation: a machine learning tool for microscopy pixel classification. *Bioinformatics*. 33:2424–2426. doi:10.1093/bioinformatics/btx180.

Bannister, L., M. Berry, P. Collins, M. Dyson, J. Dussek, and M. Ferguson. 1995. Gray's Anatomy: The anatomical basis of medicine and surgery. *In* Gray's Anatomy. Churchill Livingstone, New York. 417–424.

Chen, J.-H., F. Liao, Y. Zhang, Y. Li, C.-J. Chang, C.-P. Chou, T.-L. Yang, and M.-Y. Su. 2017. 3D MRI for Quantitative Analysis of Quadrant Percent Breast Density: Correlation with Quadrant Location of Breast Cancer. *Acad Radiol*. 24:811–817. doi:10.1016/j.acra.2016.12.016.

Chen, Y., B. Pal, G.J. Lindeman, J.E. Visvader, and G.K. Smyth. 2022. R code and downstream analysis objects for the scRNA-seq atlas of normal and tumorigenic human breast tissue. *Sci Data*. 9:96. doi:10.1038/s41597-022-01236-2.

Cheung, K.J., E. Gabrielson, Z. Werb, and A.J. Ewald. 2013. Collective Invasion in Breast Cancer Requires a Conserved Basal Epithelial Program. *Cell*. 155:1639–1651. doi:10.1016/j.cell.2013.11.029.

Dontu, G., and T.A. Ince. 2015. Of Mice and Women: A Comparative Tissue Biology Perspective of Breast Stem Cells and Differentiation. *J Mammary Gland Biol Neoplasia*. 20:51–62. doi:10.1007/s10911-015-9341-4.

Figueroa, J.D., R.M. Pfeiffer, D.A. Patel, L. Linville, L.A. Brinton, G.L. Gierach, X.R. Yang, D. Papathomas, D. Visscher, C. Mies, A.C. Degnim, W.F. Anderson, S. Hewitt, Z.G. Khodr, S.E. Clare, A.M. Storniolo, and M.E. Sherman. 2014. Terminal Duct Lobular Unit Involution of the Normal Breast: Implications for Breast Cancer Etiology. *J Natl Cancer Inst*. 106:dju286. doi:10.1093/jnci/dju286.

Fujiwara, S., S. Deguchi, and T.M. Magin. 2020. Disease-associated keratin mutations reduce traction forces and compromise adhesion and collective migration. *Journal of Cell Science*. 133:jcs243956. doi:10.1242/jcs.243956.

Gimpl, G., and F. Fahrenholz. 2001. The oxytocin receptor system: structure, function, and regulation. *Physiol Rev*. 81:629–683. doi:10.1152/physrev.2001.81.2.629.

Goldhammer, N., J. Kim, R. Villadsen, L. Rønnov-Jessen, and O.W. Petersen. 2022. Myoepithelial progenitors as founder cells of hyperplastic human breast lesions upon PIK3CA transformation. *Commun Biol*. 5:1–13. doi:10.1038/s42003-022-03161-x.

Gray, G.K., C.M.-C. Li, J.M. Rosenbluth, L.M. Selfors, N. Girnius, J.-R. Lin, R.C.J. Schackmann, W.L. Goh, K. Moore, H.K. Shapiro, S. Mei, K. D'Andrea, K.L. Nathanson, P.K. Sorger, S. Santagata, A. Regev, J.E. Garber, D.A. Dillon, and J.S. Brugge. 2022. A human breast atlas integrating single-cell proteomics and transcriptomics. *Developmental Cell*. 57:1400-1420.e7. doi:10.1016/j.devcel.2022.05.003.

Gusterson, B.A., D.T. Ross, V.J. Heath, and T. Stein. 2005. Basal cytokeratins and their relationship to the cellular origin and functional classification of breast cancer. *Breast Cancer Research*. 7:143. doi:10.1186/bcr1041.

Hannezo, E., C.L.G.J. Scheele, M. Moad, N. Drogo, R. Heer, R.V. Sampogna, J. van Rheenen, and B.D. Simons. 2017. A Unifying Theory of Branching Morphogenesis. *Cell*. 171:242-255.e27. doi:10.1016/j.cell.2017.08.026.

Hilson, J.B., S.J. Schnitt, and L.C. Collins. 2009. Phenotypic Alterations in Ductal Carcinoma In Situ-associated Myoepithelial Cells: Biologic and Diagnostic Implications. *The American Journal of Surgical Pathology*. 33:227. doi:10.1097/PAS.0b013e318180431d.

Honeth, G., T. Schiavinotto, F. Vaggi, R. Marlow, T. Kanno, I. Shinomiya, S. Lombardi, B. Buchupalli, R. Graham, P. Gazinska, V. Ramalingam, J. Burchell, A.D. Purushotham, S.E. Pinder, A. Csikasz-Nagy, and G. Dontu. 2015. Models of Breast Morphogenesis Based on Localization of Stem Cells in the Developing Mammary Lobule. *Stem Cell Reports*. 4:699–711. doi:10.1016/j.stemcr.2015.02.013.

Howard, B.A., and B.A. Gusterson. 2000. Human Breast Development. *J Mammary Gland Biol Neoplasia*. 5:119–137. doi:10.1023/A:1026487120779.

Kohler, K.T., N. Goldhammer, S. Demharter, U. Pfisterer, K. Khodosevich, L. Rønnov-Jessen, O.W. Petersen, R. Villadsen, and J. Kim. 2022. Ductal keratin 15+ luminal progenitors in normal breast exhibit a basal-like breast cancer transcriptomic signature. *npj Breast Cancer*. 8:1–12. doi:10.1038/s41523-022-00444-8.

Macias, H., and L. Hinck. 2012. Mammary gland development. *WIREs Developmental Biology*. 1:533–557. doi:10.1002/wdev.35.

Messal, H.A., J. Almagro, M. Zaw Thin, A. Tedeschi, A. Ciccarelli, L. Blackie, K.I. Anderson, I. Miguel-Aliaga, J. van Rheenen, and A. Behrens. 2021. Antigen retrieval and clearing for whole-organ immunofluorescence by FLASH. *Nature Protocols*. 16:239–262. doi:10.1038/s41596-020-00414-z.

Nelson, C.M., M.M. VanDuijn, J.L. Inman, D.A. Fletcher, and M.J. Bissell. 2006. Tissue Geometry Determines Sites of Mammary Branching Morphogenesis in Organotypic Cultures. *Science*. 314:298–300. doi:10.1126/science.1131000.

Nerger, B.A., J.M. Jaslove, H.E. Elashal, S. Mao, A. Košmrlj, A.J. Link, and C.M. Nelson. 2021. Local accumulation of extracellular matrix regulates global morphogenetic patterning in the developing mammary gland. *Curr Biol*. 31:1903-1917.e6. doi:10.1016/j.cub.2021.02.015.

Nguyen, Q.H., N. Pervolarakis, K. Blake, D. Ma, R.T. Davis, N. James, A.T. Phung, E. Willey, R. Kumar, E. Jabart, I. Driver, J. Rock, A. Goga, S.A. Khan, D.A. Lawson, Z. Werb, and K. Kessenbrock. 2018. Profiling human breast epithelial cells using single cell RNA sequencing identifies cell diversity. *Nature Communications*. 9:1–12. doi:10.1038/s41467-018-04334-1.

Osin, P.P., R. Anbazhagan, J. Bartkova, B. Nathan, and B.A. Gusterson. 1998. Breast development gives insights into breast disease. *Histopathology*. 33:275–283. doi:10.1046/j.1365-2559.1998.00479.x.

Peurla, M. 2023. 3D branching simulation v. 3.21. 1. doi:10.17632/y8d52ygdxv.1.

Ramakrishnan, R., S.A. Khan, and S. Badve. 2002. Morphological Changes in Breast Tissue with Menstrual Cycle. *Mod Pathol*. 15:1348–1356. doi:10.1097/01.MP.0000039566.20817.46.

Ramms, L., G. Fabris, R. Windoffer, N. Schwarz, R. Springer, C. Zhou, J. Lazar, S. Stiefel, N. Hersch, U. Schnakenberg, T.M. Magin, R.E. Leube, R. Merkel, and B. Hoffmann. 2013. Keratins as the main component for the mechanical integrity of keratinocytes. *Proc Natl Acad Sci U S A*. 110:18513–18518. doi:10.1073/pnas.1313491110.

Rios, A.C., B.D. Capaldo, F. Vaillant, B. Pal, R. van Ineveld, C.A. Dawson, Y. Chen, E. Nolan, N.Y. Fu, 3DTCLSM Group, F.C. Jackling, S. Devi, D. Clouston, L. Whitehead, G.K. Smyth, S.N. Mueller, G.J. Lindeman, and J.E. Visvader. 2019. Intraclonal Plasticity in Mammary Tumors Revealed through Large-Scale Single-Cell Resolution 3D Imaging. *Cancer Cell*. 35:618-632.e6. doi:10.1016/j.ccell.2019.02.010.

Roos, F.J.M., G.S. van Tienderen, H. Wu, I. Bordeu, D. Vinke, L.M. Albarinos, K. Monfils, S. Niesten, R. Smits, J. Willemse, O. Rosmark, G. Westergren-Thorsson, D.J. Kunz, M. de Wit, P.J. French, L. Vallier, J.N.M. IJzermans, R. Bartfai, H. Marks, B.D. Simons, M.E. van Royen, M.M.A. Verstegen, and L.J.W. van der Laan. 2022. Human branching cholangiocyte organoids recapitulate functional bile duct formation. *Cell Stem Cell*. 29:776-794.e13. doi:10.1016/j.stem.2022.04.011.

Rosebrock, A., J.J. Caban, J. Figueroa, G. Gierach, L. Linville, S. Hewitt, and M. Sherman. 2013. Quantitative Analysis of TDLUs using Adaptive Morphological Shape Techniques. *Proc SPIE*. 8676:86760N. doi:10.1117/12.2006619.

Russell, T.D., S. Jindal, S. Agunbiade, D. Gao, M. Troxell, V.F. Borges, and P. Schedin. 2015. Myoepithelial Cell Differentiation Markers in Ductal Carcinoma in Situ Progression. *The American Journal of Pathology*. 185:3076–3089. doi:10.1016/j.ajpath.2015.07.004.

Russo, J., R. Rivera, and I.H. Russo. 1992. Influence of age and parity on the development of the human breast. *Breast Cancer Res Treat*. 23:211–218. doi:10.1007/BF01833517.

Russo, J., A.L. Romero, and I.H. Russo. 1994. Architectural pattern of the normal and cancerous breast under the influence of parity. *Cancer Epidemiol Biomarkers Prev*. 3:219–224.

Russo, J., and I.H. Russo. 1997. Differentiation and breast cancer. *Medicina (B Aires)*. 57 Suppl 2:81–91.

Short, K., M. Hodson, and I. Smyth. 2013. Spatial mapping and quantification of developmental branching morphogenesis. *Development*. 140:471–478. doi:10.1242/dev.088500.

Silberstein, G.B. 2001. Postnatal mammary gland morphogenesis. *Microscopy Research and Technique*. 52:155–162. doi:10.1002/1097-0029(20010115)52:2<155::AID-JEMT1001>3.0.CO;2-P.

Silberstein, G.B., and C.W. Daniel. 1984. Glycosaminoglycans in the basal lamina and extracellular matrix of serially aged mouse mammary ducts. *Mech Ageing Dev*. 24:151–162. doi:10.1016/0047-6374(84)90067-8.

Silberstein, G.B., and C.W. Daniel. 1987. Reversible Inhibition of Mammary Gland Growth by Transforming Growth Factor-β. *Science*. 237:291–293. doi:10.1126/science.3474783.

Stevenson, A.J., G. Vanwalleghem, T.A. Stewart, N.D. Condon, B. Lloyd-Lewis, N. Marino, J.W. Putney, E.K. Scott, A.D. Ewing, and F.M. Davis. 2020. Multiscale imaging of basal cell dynamics in the functionally mature mammary gland. *PNAS*. doi:10.1073/pnas.2016905117.

Susaki, E.A., K. Tainaka, D. Perrin, F. Kishino, T. Tawara, T.M. Watanabe, C. Yokoyama, H. Onoe, M. Eguchi, S. Yamaguchi, T. Abe, H. Kiyonari, Y. Shimizu, A. Miyawaki, H. Yokota, and H.R. Ueda. 2014. Whole-Brain Imaging with Single-Cell Resolution Using Chemical Cocktails and Computational Analysis. *Cell*. 157:726–739. doi:10.1016/j.cell.2014.03.042.

Sznurkowska, M.K., E. Hannezo, R. Azzarelli, S. Rulands, S. Nestorowa, C.J. Hindley, J. Nichols, B. Göttgens, M. Huch, A. Philpott, and B.D. Simons. 2018. Defining Lineage Potential and Fate Behavior of Precursors during Pancreas Development. *Dev Cell*. 46:360-375.e5. doi:10.1016/j.devcel.2018.06.028.

Tabár, L., P.B. Dean, F.L. Tucker, A.M.-F. Yen, J.C.-Y. Fann, A.T.-Y. Lin, R.A. Smith, S.W. Duffy, and T.H.-H. Chen. 2022. Breast cancers originating from the terminal ductal lobular units: In situ and invasive acinar adenocarcinoma of the breast, AAB. *European Journal of Radiology*. 152:110323. doi:10.1016/j.ejrad.2022.110323.

Taylor-Papadimitriou, J., M. Stampfer, J. Bartek, A. Lewis, M. Boshell, E.B. Lane, and I.M. Leigh. 1989. Keratin expression in human mammary epithelial cells cultured from normal and malignant tissue: relation to in vivo phenotypes and influence of medium. *Journal of Cell Science*. 94:403–413. doi:10.1242/jcs.94.3.403.

Uçar, M.C., D. Kamenev, K. Sunadome, D. Fachet, F. Lallemend, I. Adameyko, S. Hadjab, and E. Hannezo. 2021. Theory of branching morphogenesis by local interactions and global guidance. *Nat Commun*. 12:6830. doi:10.1038/s41467-021-27135-5.

Villadsen, R., A.J. Fridriksdottir, L. Rønnov-Jessen, T. Gudjonsson, F. Rank, M.A. LaBarge, M.J. Bissell, and O.W. Petersen. 2007. Evidence for a stem cell hierarchy in the adult human breast. *Journal of Cell Biology*. 177:87–101. doi:10.1083/jcb.200611114.

Vince, J. 2021. Vector Analysis for Computer Graphics. Springer, London.

Wellings, S.R., H.M. Jensen, and R.G. Marcum. 1975. An Atlas of Subgross Pathology of the Human Breast With Special Reference to Possible Precancerous Lesions2. *JNCI: Journal of the National Cancer Institute*. 55:231–273. doi:10.1093/jnci/55.2.231.